PAPER

Graphene covalently functionalized with poly(*p*-phenylenediamine) as high performance electrode material for supercapacitors

Zanhui Liu,[ab] Haihui Zhou,*[ab] Zhongyuan Huang,[ab] Wenyang Wang,[ab] Fanyan Zeng[ab] and Yafei Kuang*[ab]

A reduced graphene oxide–poly(*p*-phenylenediamine) (RGO–PPD) composite was prepared from *p*-phenylenediamine (PD) and chlorinated graphene oxide (GO–COCl) sheets through amidation and polymerization processes. Then the RGO–PPD composite was characterized by using scanning electron microscopy, transmission electron microscopy and energy dispersive spectroscopy. The results show that PPD nanoparticles were wrapped within or on the surface of graphene sheets uniformly. The RGO–PPD composite displayed a layered-stacking structure and had a large surface area (674.22 m^2 g^{-1}) and a high pore volume (0.43 cm^3 g^{-1}). Capacitive properties of the RGO–PPD composite were studied using cyclic voltammetry (CV), galvanostatic charge/discharge and electrochemical impedance spectroscopy (EIS) in an electrolyte of 0.5 M H_2SO_4 aqueous solution. The RGO–PPD exhibits a high specific capacitance of 347 F g^{-1} at a discharge rate of 1 A g^{-1} and excellent cycling stability with 90.1% of its initial capacitance at a large current density of 10 A g^{-1} after 1000 charge/discharge cycles. The energy density and specific power density of the present supercapacitor are 48.2 W h kg^{-1} and 1.0 kW kg^{-1}, respectively. The results suggest that the RGO–PPD is a promising material for high-performance supercapacitor applications.

1 Introduction

Supercapacitors, also known as electrochemical capacitors (ECs), play a very important role in energy storage for electric devices and vehicles. Supercapacitors have many advantages such as long cycle life, high power density and no memory effect.[1] Based on their energy storage mechanisms ECs are divided into faradaic pseudocapacitors and double-layer electrochemical capacitors (EDLCs). Carbon materials commonly correspond to EDLCs, while conducting polymers and transition metal oxides correspond to faradaic pseudocapacitors.[2] In EDLCs, energy is stored through polarization followed by adsorption of ionic charges on the surface of electrode materials and hence the surface area of electrode materials plays a major role.[3] Nano-scale carbon materials due to the high specific surface area and good electrical conductivity are promising electrode materials for supercapacitors.[4,5] In particular, considering the energy/weight ratio and material cost, graphene is an ideal supercapacitor material due to its light weight, chemical inertness, high surface area (2630 m^2 g^{-1}), excellent conductivity and low cost.[6]

Graphene, a new carbonaceous material with a two-dimensional and single atom thick plane, shows a honeycomb lattice of a hexagonal sp^2 hybrid orbital plane film.[7] Currently, various methods have been reported to prepare graphene, such as micro-mechanical cracking,[8] epitaxial growth[9,10] and chemical exfoliation.[11,12] Considering the layer selectivity and productivity of graphene, the chemical exfoliation strategy from bulk graphite has been suggested to be an effective general method to produce graphene largely and cheaply,[13] in which the graphite oxidation process is involved in the preparation of graphene oxides (GO), and then the reduced graphene oxides (RGO) are obtained by chemical reduction of GO.[14]

In theory, RGO with a huge surface area is an ideal supercapacitor material, but the present research results showed that the actual capacitance of graphene or RGO was far away from the theoretical value.[15] The reasons could be that the changes in the composition and structure of RGO may reduce its conductivity especially when RGO was obtained by chemical reduction of GO. Moreover, the obvious irreversible agglomeration of RGO could greatly reduce the real surface area of the RGO.[16,17] Therefore, a large number of surface modification techniques for GO or RGO were developed in order to improve their dispersion capability and to prevent the aggregation of the graphene nanosheets.[18,19] Some researchers were committed to

[a]State Key Laboratory for Chemo/Biosensing and Chemometrics, Hunan University, Changsha, China. E-mail: yafeik@163.com; Fax: +86-731-88713642; Tel: +86-731-88821603

[b]College of Chemistry and Chemical Engineering, Hunan University, Changsha, China. E-mail: yafeik@163.com; Fax: +86-731-88713642; Tel: +86-731-88821603

functionalization of RGO with metal oxides,[20,21] inorganic nonmetallic materials[22] or conductive polymers[23,24] in order to overcome the bad dispersion performance of RGO.[25–28] However, these kinds of non-covalent approaches may have some disadvantages, such as slippage of the molecules, and they are hard to control and unstable compared to the covalent approach.[29] Therefore, the covalent modification strategy is a more promising way for this purpose. Many research results have been achieved in the functionalized modification of GO or RGO by combining them with certain molecules or functional groups mostly in order to solve the dispersion property in a specific medium.[29–31] However, the ways of reducing the agglomeration of RGO and use its real surface area more efficiently to take full advantage of the capacitive behavior are seldom mentioned in the literature.

Graphene oxide (GO) exhibits tremendous positive edges and plentiful oxygen-containing functional groups on its basal plane, providing compatibility with polymer matrices[32] when used as a composite matrix material by controllable amidation reaction. Additionally, the conductivity of graphene can be greatly improved after it is functionalized *via* aryl groups.[33,34] *p*-Phenylenediamine (PD), a simple aromatic diamine, can be used as a reducing reagent in the preparation of RGO, which was effective to overcome the aggregation.[35] Herein, we report for the first time the preparation and performance of the RGO–PPD composite as an electrode material for supercapacitors. We use the bridging role of the PPD as a scaffold for supporting RGO to retain the large surface area of the composite. The composite was synthesized by grafting a PD monomer to chlorinated graphene oxide (GO–COCl) sheets through amidation, followed by polymerization and reduction processes. The effect of the loading of the PPD polymer on the capacitive performance of the RGO–PPD composite was also investigated. The composite showed excellent capacitance performance as an electrode material for supercapacitors because of its high efficiency of charge transfer. The maximum specific capacitance of 347 F g^{-1} can be obtained at a discharge rate of 1 A g^{-1}.

2 Experimental

2.1 Chemicals and materials

Natural graphite flakes (99.8%) were obtained from Alfa Aesar. Tetrahydrofuran (THF) was distilled prior to use. *N,N*-Dimethylformamide (DMF) was purified under vacuum. *p*-Phenylenediamine (PD), thionyl chloride (SOCl$_2$), triethylamine (Et$_3$N) and other solvents were obtained from Sinopharm Chemical Reagent Co., Ltd. and used as received. Deionized water was used for preparation and dilution purposes.

2.2 Chlorinated graphene oxide (GO–COCl)

Graphene oxide (GO) was prepared from natural graphite sheets using a modified Hummers' method.[36,37] In order to obtain the best possible degree of oxidation of GO by prolonging the oxidation time and increasing the oxidant amount, GO (600 mg) was reacted with 35 mL SOCl$_2$ (containing 1 mL of DMF) at 80 °C

for 24 h under nitrogen atmosphere reflux to convert the carboxyl groups into acyl chlorides.[38] At the end of the reaction, the remaining thionyl chloride and solvent were removed by distillation. And the chlorinated graphene oxide (GO–COCl) was centrifuged and washed with distilled tetrahydrofuran (THF). Lastly, the GO–COCl was stored under vacuum.

2.3 Functionalized graphene (RGO–PPD)

Typically, PD monomer and Et$_3$N (100 μL) were added into a suspension of GO–COCl (20 mg) in anhydrous DMF (20 mL), and subsequently, the reaction mixture was refluxed at 80 °C for 24 h under nitrogen. After that, the excess PD was polymerized chemically by ammonium persulfate (APS) under intense stirring at 3 °C for 2 h. Subsequently, the unreacted oxygen-containing groups were reduced by sodium borohydride (NaBH$_4$) for preparing RGO–PPD. The RGO–PPD composite was separated by repeated centrifugation and washed with water. Four different mass ratios (GO–COCl/PD = 1/5, 1/2, 5/1, 10/1) were investigated. For comparison, pure PPD without RGO was prepared by the oxidation of PD in DMF solution by APS, and RGO was also obtained by reducing GO–COCl with NaBH$_4$.

2.4 Instruments and measurements

Thermal gravimetric analysis (TGA) was carried out on a NETZSCH-409PC TGA instrument at a heating rate of 10 °C min^{-1} from room temperature to 800 °C under a nitrogen atmosphere. Ultraviolet-visible (UV-vis) spectra measurements were performed on the TechLab UV-2100 ultraviolet and visible spectrophotometer. Fourier-transform infrared (FTIR) spectra were recorded on a NICOLET 6700 FTIR spectrometer (KBr disk). The morphologies of the composite were characterized using a scanning electron microscope (SEM, Hitachi S-4800) and a transmission electron microscope (TEM, JEOL 3010). The element analysis was conducted using an energy-dispersive X-ray spectroscopy (EDS) analyzer mounted on the JEOL-3010. The pore structure of materials was characterized by N$_2$ sorption measurements on the SA-3100 (BECKMAN COULTER).

All electrochemical measurements were carried out with an electrochemical working station (CHI660C, Chenhua Inc., China) at room temperature in an open three-electrode cell system. The modified glassy carbon electrodes (GC, s = 0.1256 cm^2) were used as the working electrodes. A platinum wire and a saturated calomel electrode (SCE) were used as the auxiliary and reference electrodes, respectively. In all electrochemical experiments, the electrolyte used was 0.5 M H$_2$SO$_4$ aqueous solution. The capacitive performance of electrodes was measured using cyclic voltammetry (CV), galvanostatic charge/discharge and electrochemical impedance spectroscopy (EIS).

3 Results and discussion

Our basic strategy to synthesize RGO–PPD involves three steps, and a schematic illustration is presented in Fig. 1. Firstly, chlorinated graphene oxide (GO–COCl) was obtained by the reaction between GO sheets and thionyl chloride (SOCl$_2$).
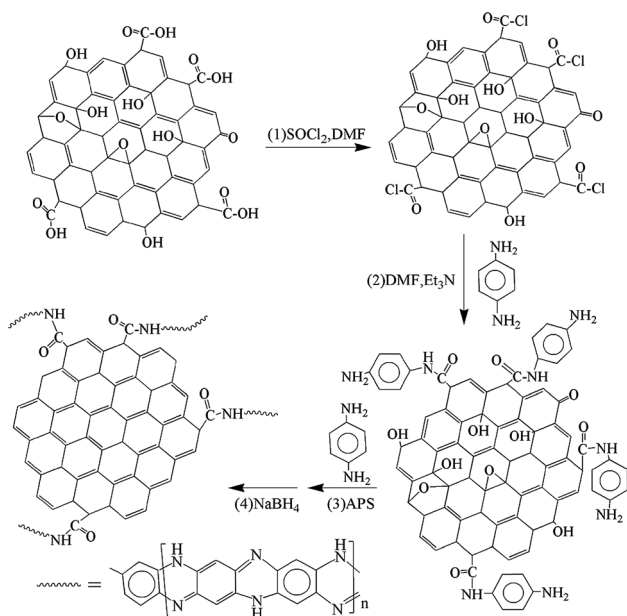
Fig. 1 Schematic illustration of the synthesis of the RGO–PPD composite.

Secondly, PD was covalently immobilized onto the GO–COCl and subsequently polymerized to form GO–PPD. Finally, the GO–PPD was reduced by sodium borohydride (NaBH₄) to obtain the final product RGO–PPD.

Fig. 2 shows the UV-vis absorption spectra of PPD, GO–COCl and RGO–PPD in DMF. The PPD exhibits two typical absorption peaks at around 272 and 422 nm. The first absorption band in the region of around 272 nm is assigned to the π–π* transition of the benzenoid ring of the polymer. The second absorption band at around 422 nm is due to the electronic transition of quinoid imine structures which may be assigned to PPD segments. The GO–COCl spectrum exhibits absorption at 266 nm due to the π-conjugated network within the graphene sheets. Similar characteristic bands are also observed for

RGO–PPD, and the spectrum of the RGO–PPD suspension in DMF shows a blueshift of the absorption peak to 265 nm upon reduction. This result shows that the restoration of the π-conjugated network within the graphene sheets occurred upon chemical reduction. Furthermore, the spectrum of the RGO–PPD exhibits a new broad absorption peak at 571 nm, which may be due to the interaction between the graphene and the polymer chains.

The thermal stability of GO, PPD, GO–COCl and RGO–PPD (5/1) is shown in Fig. 3. For the TGA curve of GO, there are two main stages of weight loss before 200 °C in a N₂ atmosphere due to the removal of adsorbed water and oxygen containing groups.[39] For the PPD, the main stage of weight loss starting from 170 °C is attributed to the decomposition of the polymer. PPD has an ordered structure due to *ortho*- and *para*-position polymerization, thus demonstrating the relatively good thermal stability. For the GO–COCl and RGO–PPD, the shapes of the TGA curves are similar to each other, and a slow weight loss may be because most of the oxygen functional groups have been removed during the chloride process.[40] This suggests that the addition of RGO–PPD improved the thermal stability of the polymer.

FTIR is a powerful tool to analyze compositions of materials. Fig. 4 shows the FTIR spectra of GO, GO–COCl, PPD and RGO–PPD. In the FTIR spectrum of GO as shown in Fig. 4(a), the following functional groups were identified: –OH groups centered at 3435 cm^{-1}, –CH₂– at 2920 cm^{-1}, C–H stretch of –CH₃ at 2845 cm^{-1}, C=O stretching at 1735 cm^{-1}, aromatic C=C stretching vibration at 1625 cm^{-1}, O–H deformation vibration at 1399 cm^{-1} and the alkoxy C–O stretching vibration at 1052 cm^{-1}. The bands at 1230 cm^{-1} and 833 cm^{-1} can be attributed to the symmetrical and asymmetrical stretching vibration of epoxy C–O–C groups. The FTIR spectrum of GO–COCl (Fig. 4(b)) exhibits that it still retains oxygen-containing functional groups. However, the relative intensity of the C=O stretch of the –COOH at 1730 cm^{-1} has significantly decreased, confirming that most
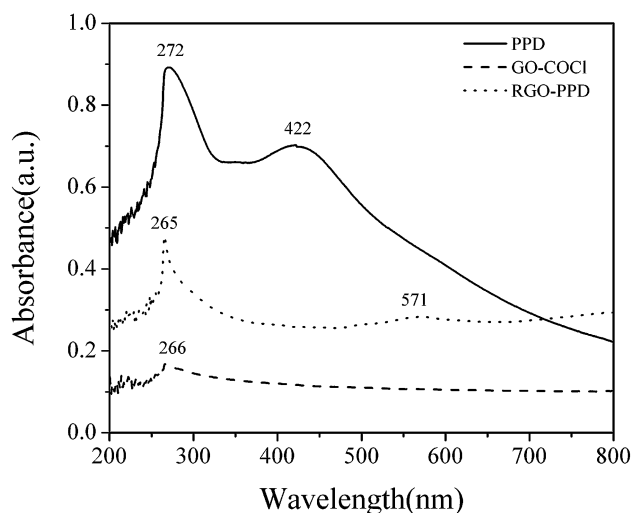

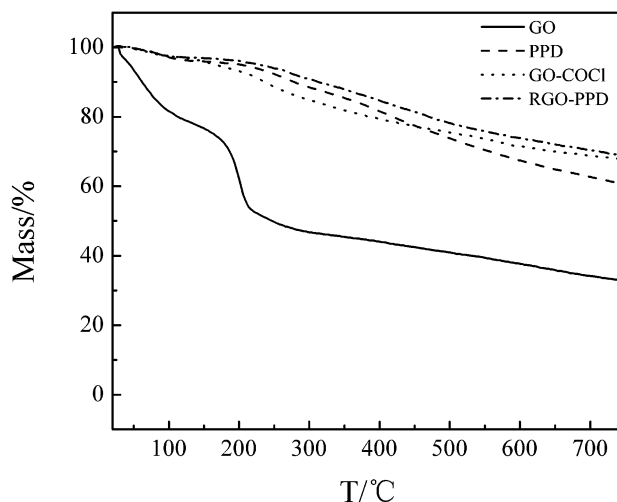**Fig. 2** UV-vis absorption spectra of PPD, GO–COCl and RGO–PPD in DMF.

Fig. 3 TGA profiles of GO, PPD, GO–COCl and RGO–PPD showing the thermal stability of the composite.

3456 | *J. Mater. Chem. A*, 2013, **1**, 3454–3462

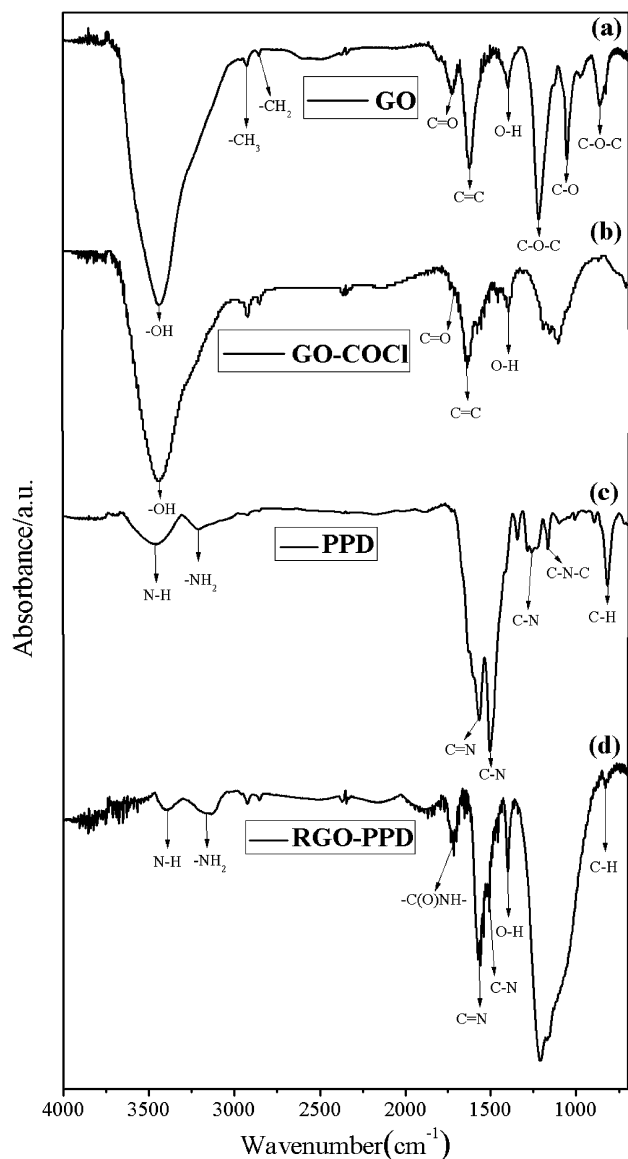This journal is © The Royal Society of Chemistry 2013

Fig. 4 FT-IR transmittance spectra of GO (a), GO–COCl (b), PPD (c) and RGO–PPD (d).

carboxyl functionalities have been transformed into acyl chloride. From the FTIR spectrum of PPD (Fig. 4(c)), two bands with maxima at 3420 cm^{-1} and 3208 cm^{-1} can be assigned to the secondary amine stretching and to terminal primary amine group vibrations in terms of N–H stretching, the strong band at 1510 cm^{-1} is due to the stretching of benzene ring skeleton vibration, and the absorption peak at 1572 cm^{-1} is consistent with the presence of quinine diimine units in the proposed structure for PPD. The benzene ring on the C–N–C and the quinoid structure in the C=N– are located at 1166 cm^{-1} and 1260 cm^{-1}. The aromatic ring C–H out-of-plane deformation vibration of the 1,4-disubstituted benzene ring is located at 825 cm^{-1}. The peaks reported here are consistent with the literature.[41] After the amidation reaction, the characteristic band of amide (–C(O)NH–) stretching vibration at 1712 cm^{-1} appears (shown in Fig. 4(d)), indicating that the PPD is covalently attached to RGO. Moreover, amine group vibration at 3415 cm^{-1}

and 3202 cm^{-1} and C–N and C=N stretching vibration at 1260 cm^{-1} and 1166 cm^{-1} observed in Fig. 4(d) are also ascribed to the PPD. After reduction, the –OH peak disappeared. This result confirmed that GO has been well deoxygenated after reduction, which is consistent with the results of TGA (Fig. 3) analysis. Taken together, UV-vis, TGA and FTIR data suggest that oxide graphene sheets were covalently functionalized with the bridge grafting of PPD. In addition, after reduction, most of the oxygen functional groups can be removed.

The morphologies of RGO, PPD and RGO–PPD are shown in Fig. 5. From Fig. 5(a), it can be observed that the RGO presented wavy wrinkles which may be caused by the combination of multi-sheet stacks and a single sheet during the preparation of GO.[42] The PPD (Fig. 5(b)) indicates spherical particles with a rough surface. The RGO–PPD (Fig. 5(c)) displays a layered-stacking structure of thick graphene sheets, and it also obviously shows that the polymer particles are uniformly and firmly bonded to graphene sheets by surface polymerization. So the surface is rougher and thicker than RGO. Fig. 5(d) shows the panorama of RGO–PPD, crumpled sheets closely associated with each other. There are a lot of interspaces between the graphene layers, providing a large surface area of RGO–PPD. Fig. 5(e) indicates the TEM image of RGO, which exhibits flat sheets overlapping with adjacent sheets. Fig. 5(f) shows that the PPD spherical particles are wrapped within or on the surface of graphene sheets. It can be seen clearly that the interlayer distance of RGO–PPD sheets is evidently larger than that of RGO sheets. Herein, RGO–PPD sheets are still largely in a planar state and
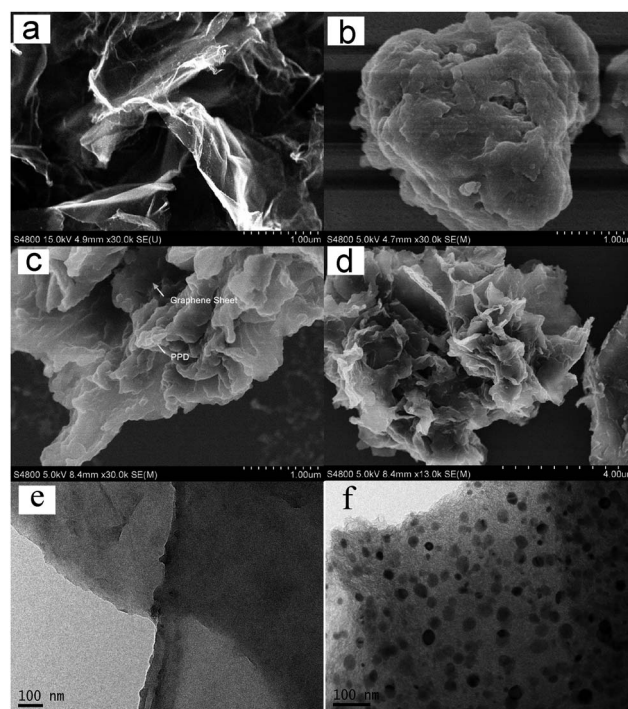

Fig. 5 SEM images of (a) RGO, (b) PPD, and (c) high-magnified and (d) low-magnified cross-sections of RGO–PPD. TEM images of (e) RGO and (f) RGO–PPD.

extensively decorated by PPD. These results agree with the SEM images well.

The EDS pattern of RGO–PPD is strong evidence to authenticate the composition of the RGO–PPD. Fig. 6 shows the existence of N, S, Cl and Si elements in addition to C and O elements. The N signal is originated from PPD. The S and Cl signals are originated from SOCl$_2$ and the Si signal is originated from the silicon base. Fig. 7 shows the surface area changes and the pore size distributions of RGO and RGO–PPD. According to the IUPAC classification, it can be observed that the N$_2$ sorption isotherms are of type IV from Fig. 7(a), which suggests the porous characteristics of RGO–PPD. The specific surface area and total pore volume obtained are typically $S_{BET} = 674.22$ m^2 g^{-1} and $V_t = 0.43$ cm^3 g^{-1} for RGO–PPD, which are much higher than $S_{BET} = 45.60$ m^2 g^{-1} and $V_t = 0.18$ cm^3 g^{-1} for RGO, which might be attributed to good incorporation and dispersion of PPD on the surface of carbonaceous nanosheets in the basic media. Fig. 7(b) indicates that RGO–PPD is a porous material and the pore size of RGO–PPD is around 3–4 nm. However, the pore volume of RGO is much less than that of RGO–PPD.

Cyclic voltammetry (CV) is an effective method to determine faradaic and nonfaradaic behavior and assess capacitive performance. Fig. 8 shows the CV curves of PPD, RGO and RGO–PPD (5/1) modified GC electrodes in 0.5 M H$_2$SO$_4$ at a scan rate of 100 mV s^{-1}. It is observed that the CV curves of RGO and RGO–PPD show a rectangular shape, indicating ideal capacitive behavior. The specific capacitance was calculated using the equation below:

$$C = \frac{Q}{m\Delta V} \quad (1)$$

where Q and m are the charge and mass of the electroactive material, respectively, and V is the scan rate. According to the CV curves shown in Fig. 8, the specific capacitance values of PPD, RGO and RGO–PPD (5/1) are 66, 144 and 342 F g^{-1}, respectively. The results show that the pure PPD has low specific capacitance; however, the RGO–PPD displays the largest capacitance possibly due to the interfacial effect of the graphene
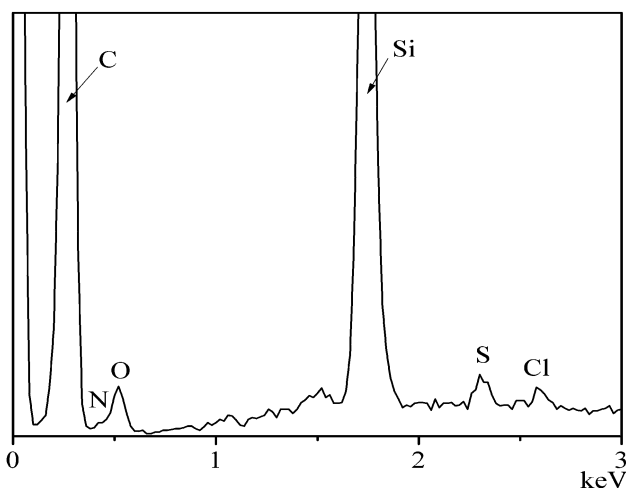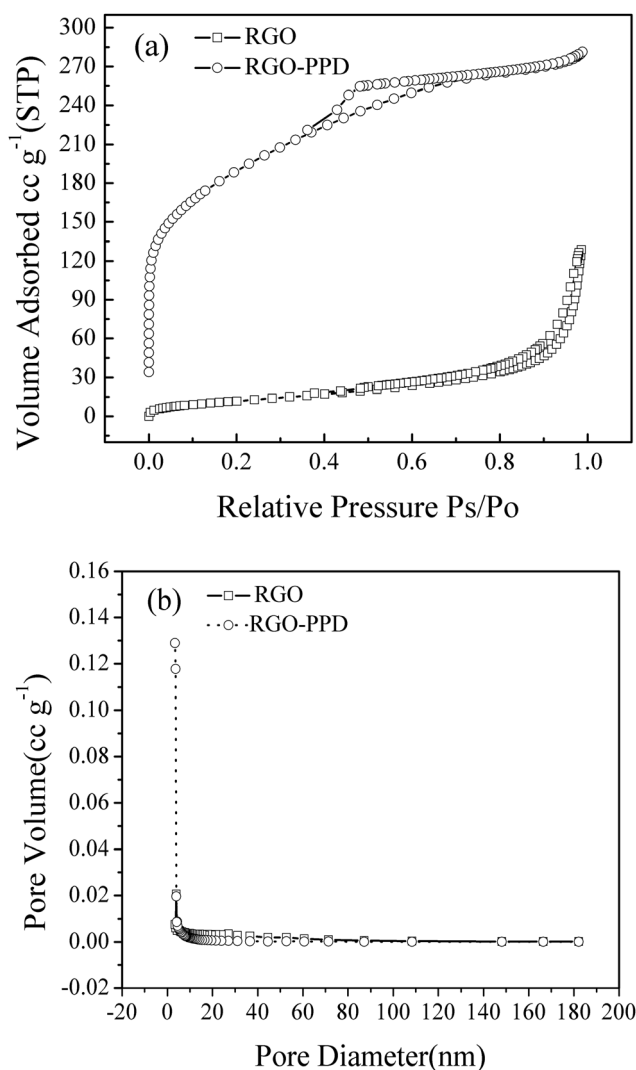

Fig. 7 (a) Nitrogen sorption isotherms. (b) Pore size distributions calculated using the BJH method.

sheets, which effectively increases the number of shortest and directional ion transport paths.[3] In addition, due to the different contributions of RGO and PPD in the composite to the capacitance, there should be a suitable mass ratio of RGO to PPD of the composite that displays the best capacitance value due to the synergistic effect of RGO and PPD; therefore, the effect of the mass ratio of RGO to PPD on capacitive performance was also studied.

Fig. 9 indicates the CV of RGO–PPD with different mass ratios (1/5, 1/2, 5/1, 10/1) at a scan rate of 100 mV s^{-1}. It shows that the RGO–PPD with a mass ratio of 5/1 possesses a maximum specific capacitance characteristic.

Fig. 10 shows the galvanostatic charge/discharge profiles of RGO–PPD with different mass ratios (RGO/PPD = 1/5, 1/2, 5/1, 10/1) at a current of 1×10^{-5} A. The linear symmetric charging and discharging curve indicates that the capacitive behavior of RGO–PPD is fully reversible.[23] The discharge curves are linear in the whole potential range with a constant slope, showing a near perfect capacitive behavior. The specific capacitance was
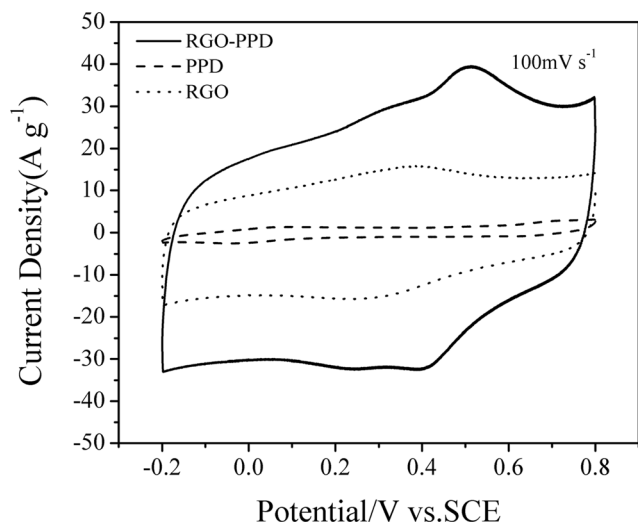

Fig. 6 EDS data of RGO–PPD.

3458 | J. Mater. Chem. A, 2013, 1, 3454–3462

This journal is © The Royal Society of Chemistry 2013

Fig. 8 CV profiles of PPD, RGO and RGO–PPD (5/1) composite electrodes measured at a scan rate of 100 mV s^{-1}.

Fig. 9 CV profiles of composite electrodes of different mass ratios at a scan rate of 100 mV s^{-1}.

calculated from the charge–discharge curve according to the following equation:

$$C = \frac{I\Delta t}{m\Delta U} \qquad (2)$$

where C is the specific capacitance (F g^{-1}), I is the current (A), Δt is the discharge time (s), m is the mass of the electroactive material (g) and ΔU is the potential change during the discharge process (V). The specific capacitance was calculated from the slope of the charge–discharge curves and the results are 178, 185, 347 and 205 F g^{-1}, respectively. The RGO–PPD composite with a mass ratio of 5/1 possesses the highest specific capacitance. So the mass ratio of 5/1 was chosen to prepare the RGO–PPD composite for further studies.

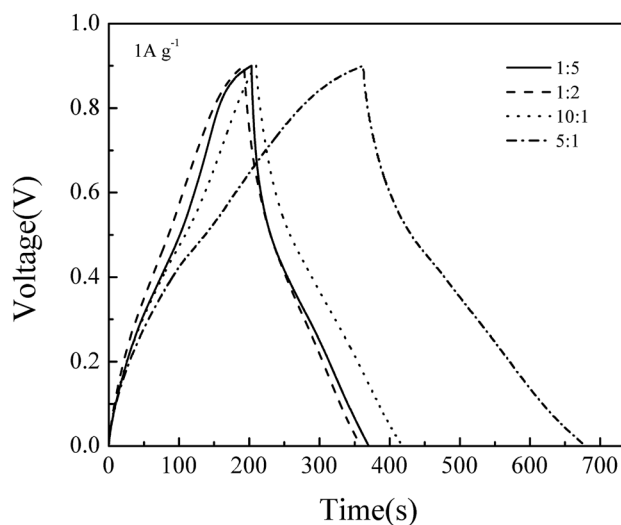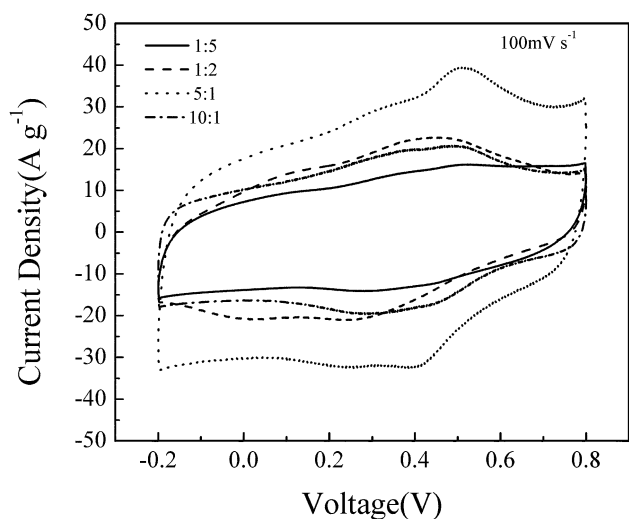Fig. 11 indicates the CV curves of RGO–PPD at different scan rates; all the CV curves still show a rectangular-like shape,

Fig. 10 Galvanostatic charge/discharge profiles of composite electrodes of different mass ratios at a current density of 1 A g^{-1}.

indicating an excellent super-capacitor behavior and a low internal resistance.

Fig. 12 shows the galvanostatic charge/discharge profiles of RGO–PPD at a constant current density of 1 A g^{-1}. The specific capacitance was calculated to be 347 F g^{-1} at 1 A g^{-1}. Similar studies were carried out for the other two samples (PPD and RGO), and they gave lower specific capacitance of 68 F g^{-1} and 152 F g^{-1}, respectively, which is consistent with the results of CV curves (Fig. 8).

Fig. 13 indicates the galvanostatic charge/discharge tests at current densities of 0.5, 1, 2, 5, and 10 A g^{-1}. As shown in Fig. 13(a), all the charge–discharge curves show relatively ideal capacitive behavior observed by the rate of change in current. Fig. 13(b) shows the specific capacitance of the RGO–PPD as a function of charge–discharge current. The increase in current
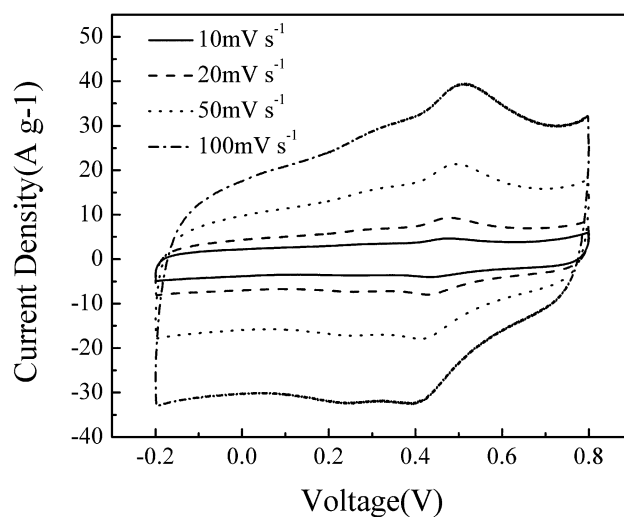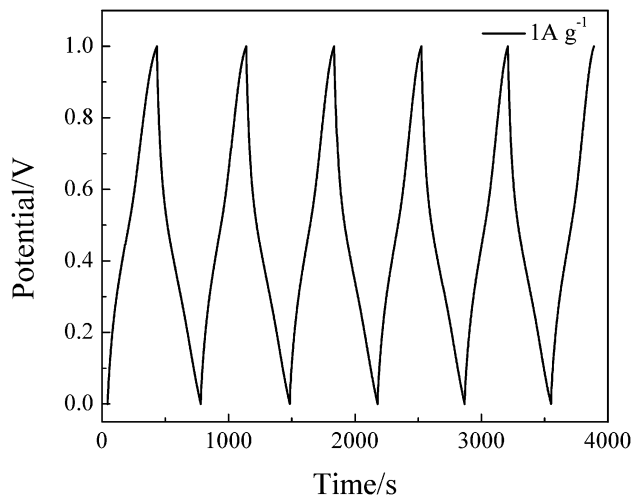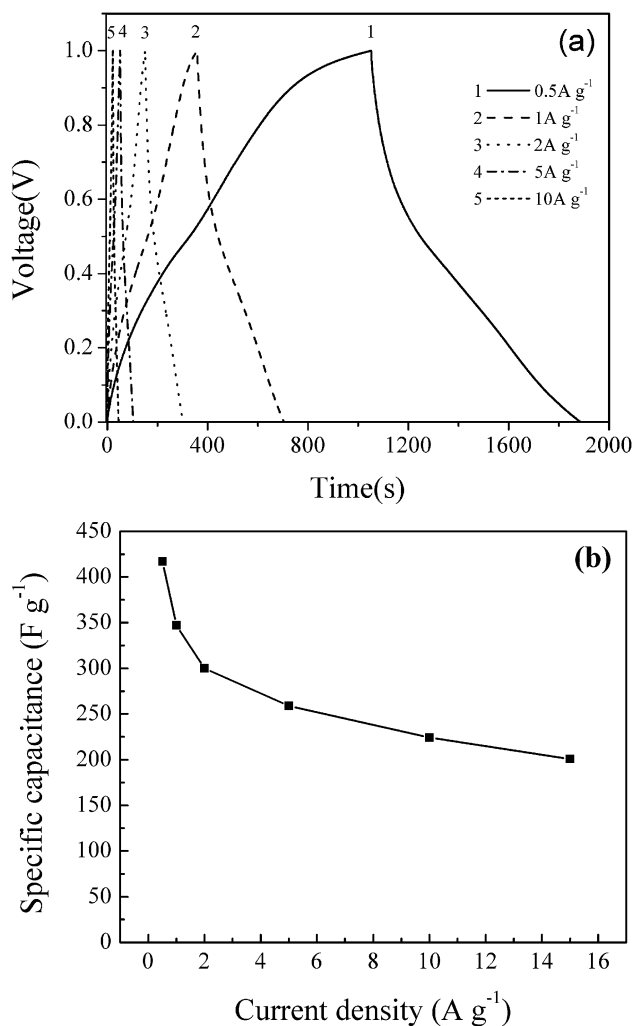

Fig. 11 CV profiles of the RGO–PPD composite electrode at a scan rate of 10, 20, 50 and 100 mV s^{-1}.

Fig. 12 Galvanostatic charge/discharge profiles of the RGO–PPD composite electrode at a current density of 1.0 A g^{-1}.

led to the decline in capacitance due to the rapid motion of massive ions, which results from the poor accommodation of ions inside the interspaces of the active electrode material. At a high current, ions may not be able to get enough time to spread into the interspaces of the active electrode material. The long cycle life of the super-capacitor is significant for its practical applications.

Fig. 14 indicates the cyclic stability of the RGO–PPD with charge–discharge cycles, which clearly shows that the specific capacitance still remains around 90.1% of its initial capacitance after 1000 cycles with a constant current density of 10 A g^{-1}. This illustrates that the RGO–PPD possesses good stability, long lifetime and a very high degree of reversibility in the repetitive charge–discharge cycling. Interestingly, the specific capacitance of the composite electrode can be further strengthened in the initial period. This activation process may result from the more complete embedding and deintercalation of electrochemical species.[20] The energy density (E) and specific power density (P) of the RGO–PPD can be calculated using the equation $E = CU^2/2$ and $P = IU/m$ respectively, where C is the capacitance and U is the cell voltage.[26] The energy density and specific power density were calculated to be 48.2 W h kg^{-1} and 1.0 kW kg^{-1}, respectively.

Further electrochemical impedance spectroscopy (EIS) was employed to understand the electrode processes. EIS was conducted at a frequency range of 100 kHz to 0.01 Hz at 0.4 V with an AC perturbation of 5 mV. As shown in the Nyquist plot (Fig. 15), a semicircle, observed in the high frequency region, is related to the electron-transfer process at the interface between RGO–PPD and the electrolyte. The equivalent series resistance (ESR) of the RGO–PPD electrode was extracted to be 10.0 ohm, indicating a low charge-transfer resistance. A linear line with a slope of 45° was observed in the middle frequency region, which is due to the Warburg resistance related to the dependence of ion diffusion. In the low frequency region, a nearly vertical line can be observed, indicating an ideal capacitance behavior.[43]

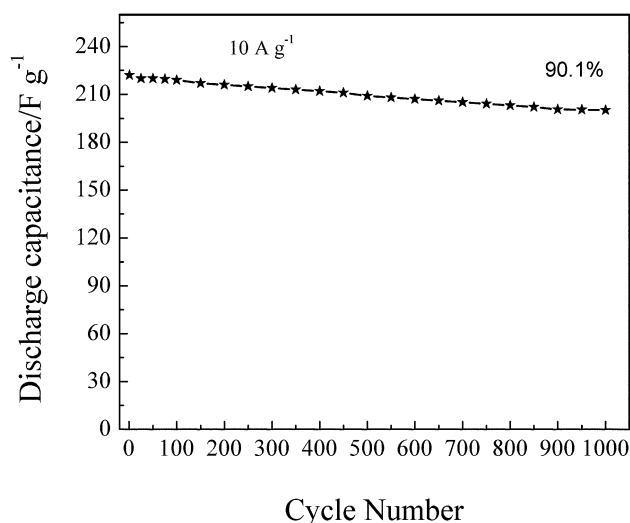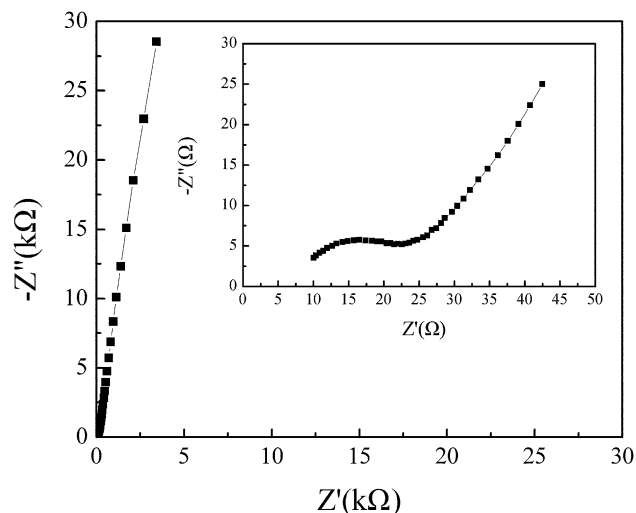

Fig. 13 (a) Galvanostatic charge/discharge curves of RGO–PPD at current densities of 0.5, 1, 2, 5, and 10 A g^{-1}. (b) Specific capacitance of the RGO–PPD as a function of current density.

Fig. 14 Cyclic stability of the composite at a current density of 10 A g^{-1}.

3460 | *J. Mater. Chem. A*, 2013, **1**, 3454–3462

This journal is © The Royal Society of Chemistry 2013

Fig. 15 Nyquist plots of the RGO–PPD composite electrode. The inset shows a magnified plot for RGO–PPD near the origin.

4 Conclusions

In conclusion, we present a controllable method for fabricating RGO–PPD composite material with enhanced performance for supercapacitors. The test results suggest that the composites have excellent supercapacitor properties due to poly(p-phenylenediamine) nanoparticles wrapped within or on the surface of graphene sheets. The nanoparticles facilitate the layered-stacking and lead to the large surface area and high pore volume of RGO. The specific capacitance of the composite was 347 F g^{-1} at a discharge rate of 1 A g^{-1}. Furthermore, the capacitance of the RGO–PPD composite remains about 90.1% of the original capacitance at a large current density of 10 A g^{-1} after 1000 charge–discharge cycles. These results demonstrate the exciting potential of the RGO–PPD composite for high-performance supercapacitors.

Acknowledgements

Notes and references

1 W. W. Liu, X. B. Yan, J. W. Lang and Q. J. Xue, *J. Mater. Chem.*, 2011, **21**, 13205–13212.

2 M. A. Pope, C. Punckt and I. A. Aksay, *J. Phys. Chem. C*, 2011, **115**, 20326–20334.

3 P. Tamailarasan and S. Ramaprabhu, *J. Phys. Chem. C*, 2012, **116**, 14179–14187.

4 H. Niu, J. Zhang, Z. Xie, X. Wang and T. Lin, *Carbon*, 2011, **49**, 2380–2388.

5 H. M. Chen, Y. Li, Y. Y. Feng, P. Lv, P. Zhang and W. Feng, *Electrochim. Acta*, 2012, **60**, 449–455.

6 M. Pumera, *Energy Environ. Sci.*, 2011, **4**, 668–674.

7 F. Du, D. S. Yu, L. M. Dai, S. Ganguli, V. Varshney and A. K. Roy, *Chem. Mater.*, 2011, **23**, 4810–4816.

8 K. S. Novoselov, A. K. Geim, S. V. Morozov, D. Jiang, Y. Zhang, S. V. Dubonos, I. V. Grigorieva and A. A. Firsov, *Science*, 2004, **306**, 666–669.

9 T. Gao, S. Xie, Y. Gao, M. Liu, Y. Chen, Y. Zhang and Z. Liu, *ACS Nano*, 2011, **5**, 9194–9201.

10 R. He, L. Zhao, N. Petrone, K. S. Kim, M. Roth, J. Hone, P. Kim, A. Pasupathy and A. Pinczuk, *Nano Lett.*, 2012, **12**, 2408–2413.

11 Z.-S. Wu, W. Ren, L. Gao, B. Liu, C. Jiang and H.-M. Cheng, *Carbon*, 2009, **47**, 493–499.

12 I. K. Moon, J. Lee and H. Lee, *Chem. Commun.*, 2011, **47**, 9681–9683.

13 S. Stankovich, D. A. Dikin, R. D. Piner, K. A. Kohlhaas, A. Kleinhammes, Y. Jia, Y. Wu, S. T. Nguyen and R. S. Ruoff, *Carbon*, 2007, **45**, 1558–1565.

14 B. Dai, L. Fu, L. Liao, N. Liu, K. Yan, Y. Chen and Z. Liu, *Nano Res.*, 2011, **4**, 434–439.

15 Y. Zhu, S. Murali, M. D. Stoller, K. J. Ganesh, W. Cai, P. J. Ferreira, A. Pirkle, R. M. Wallace, K. A. Cychosz, M. Thommes, D. Su, E. A. Stach and R. S. Ruoff, *Science*, 2011, **332**, 1537–1541.

16 K. Jo, T. Lee, H. J. Choi, J. H. Park, D. J. Lee, D. W. Lee and B. S. Kim, *Langmuir*, 2011, **27**, 2014–2018.

17 S. T. Yang, Y. Chang, H. Wang, G. Liu, S. Chen, Y. Wang, Y. Liu and A. Cao, *J. Colloid Interface Sci.*, 2010, **351**, 122–127.

18 K. P. Liu, J. J. Zhang, F. F. Cheng, T. T. Zheng, C. M. Wang and J. J. Zhu, *J. Mater. Chem.*, 2011, **21**, 12034–12040.

19 S. J. Wang, Y. Geng, Q. Zheng and J.-K. Kim, *Carbon*, 2010, **48**, 1815–1823.

20 X. C. Dong, H. Xu, X. W. Wang, Y. X. Huang, M. B. Chan-Park, H. Zhang, L. H. Wang, W. Huang and P. Chen, *ACS Nano*, 2012, **6**, 3206–3213.

21 B. G. Choi, M. Yang, W. H. Hong, J. W. Choi and Y. S. Huh, *ACS Nano*, 2012, **6**, 4020–4028.

22 Z. D. Huang, B. A. Zhang, S. W. Oh, Q. B. Zheng, X. Y. Lin, N. Yousefi and J. K. Kim, *J. Mater. Chem.*, 2012, **22**, 3591–3599.

23 L. Lai, H. Yang, L. Wang, B. K. Teh, J. Zhong, H. Chou, L. Chen, W. Chen, Z. Shen, R. S. Ruoff and J. Lin, *ACS Nano*, 2012, **6**, 5941–5951.

24 J. Zhang and X. S. Zhao, *J. Phys. Chem. C*, 2012, **116**, 5420–5426.

25 A. P. Yu, I. Roes, A. Davies and Z. W. Chen, *Appl. Phys. Lett.*, 2010, **96**, 253103–253105.

26 C. Fu, Y. Kuang, Z. Huang, X. Wang, Y. Yin, J. Chen and H. Zhou, *J. Solid State Electrochem.*, 2011, **15**, 2581–2585.

27 F. Y. Zeng, Y. F. Kuang, Y. Wang, Z. Y. Huang, C. P. Fu and H. H. Zhou, *Adv. Mater.*, 2011, **23**, 4929–4932.

28 M. D. Stoller, C. W. Magnuson, Y. W. Zhu, S. Murali, J. W. Suk, R. Piner and R. S. Ruoff, *Energy Environ. Sci.*, 2011, **4**, 4685–4689.

29 J. Q. Liu, J. G. Tang and J. J. Gooding, *J. Mater. Chem.*, 2012, **22**, 12435–12452.

30 T. Kuila, S. Bose, A. K. Mishra, P. Khanra, N. H. Kim and J. H. Lee, *Prog. Mater. Sci.*, 2012, **57**, 1061–1105.

31 D. R. Dreyer, S. Park, C. W. Bielawski and R. S. Ruoff, *Chem. Soc. Rev.*, 2010, **39**, 228–240.

32 N. A. Kumar, H. J. Choi, Y. R. Shin, D. W. Chang, L. Dai and J. B. Baek, *ACS Nano*, 2012, **6**, 1715–1723.

33 P. Huang, H. R. Zhu, L. Jing, Y. L. Zhao and X. Y. Gao, *ACS Nano*, 2011, **5**, 7945–7949.

34 H. K. He and C. Gao, *Chem. Mater.*, 2010, **22**, 5054–5064.

35 Y. Chen, X. Zhang, P. Yu and Y. Ma, *Chem. Commun.*, 2009, 4527–4529.

36 L. Zhang, J. Liang, Y. Huang, Y. Ma, Y. Wang and Y. Chen, *Carbon*, 2009, **47**, 3365–3368.

37 X. Wang, H. Bai and G. Shi, *J. Am. Chem. Soc.*, 2011, **133**, 6338–6342.

38 J. Yang, J. Li, X. Yang, X. Wang, L. Wan and Y. Yang, *Mater. Chem. Phys.*, 2012, **135**, 687–693.

39 Y. Liu, R. J. Deng, Z. Wang and H. T. Liu, *J. Mater. Chem.*, 2012, **22**, 13619–13624.

40 R. L. D. Whitby, A. Korobeinyk and K. V. Glevatska, *Carbon*, 2011, **49**, 722–725.

41 V. M. Mencatelli and P. s.n.c, *Eur. Polym. J.*, 1996, **32**, 43–50.

42 W. Zhu, T. Low, V. Perebeinos, A. A. Bol, Y. Zhu, H. Yan, J. Tersoff and P. Avouris, *Nano Lett.*, 2012, **12**, 3431–3436.

43 F. Zeng, Y. Kuang, G. Liu, R. Liu, Z. Huang, C. Fu and H. Zhou, *Nanoscale*, 2012, **4**, 3997–4001.